Supporting Information

A flexible and fully integrated wearable pressure sensing chip system for multi-scenario applications

Bo Peng [a], Xinyue Wu [a], Chao Zhang [a], Chi Zhang [a], Lingyi Lan [a], Chuanfang (John) Zhang [b,*], Yibin Ying [a], Jianfeng Ping [a,*]

[a] Laboratory of Agricultural Information Intelligent Sensing, School of Biosystems Engineering and Food Science, Zhejiang University, Hangzhou, Zhejiang 310058, China

[b] Laboratory for Functional Polymers, Swiss Federal Laboratories for Materials Science and Technology (Empa), ETH Domain, Überlandstrasse 129, CH-8600 Dübendorf, Switzerland

Corresponding author: Prof. Chuanfang (John) Zhang, Prof. Jianfeng Ping

E-mail: chuanfang.zhang@empa.ch; jfping@zju.edu.cn

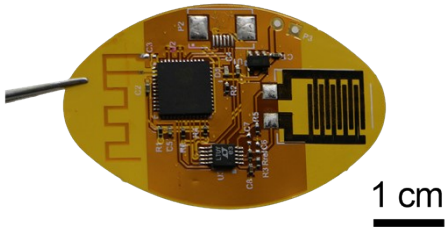

Figure S1. The FPCB and the interdigitated electrode based on PI film.

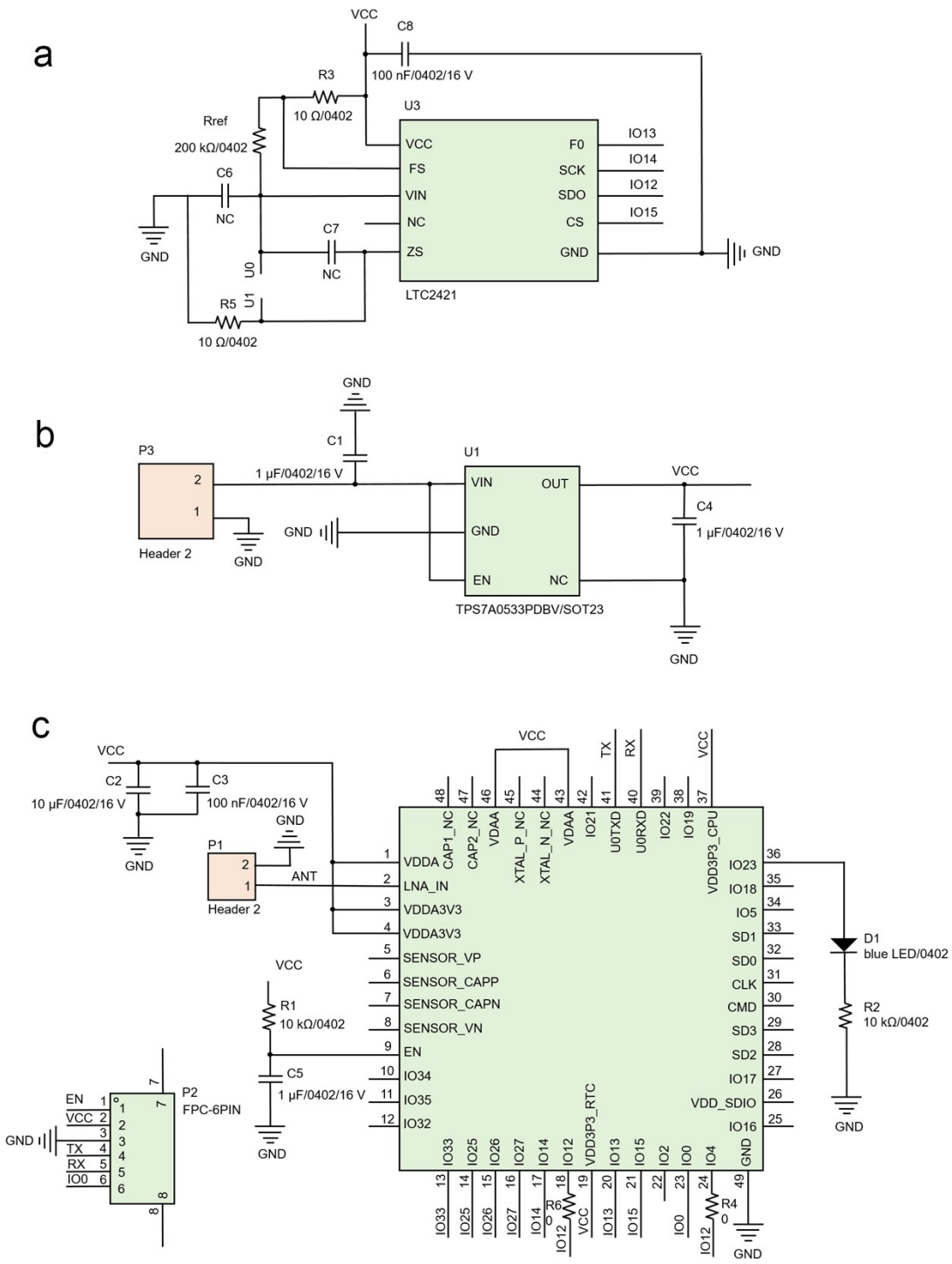

Figure S2. Schematic diagram of the circuit.

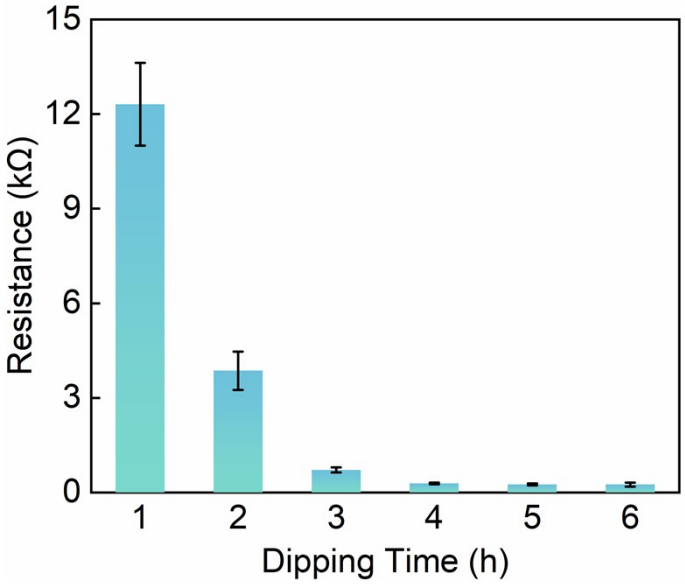

Figure S3. Resistance of the MX@Sponge under different immersing time in MXene aqueous solution. The resistance of MX@Sponge becomes stable after 4-hour immersion.

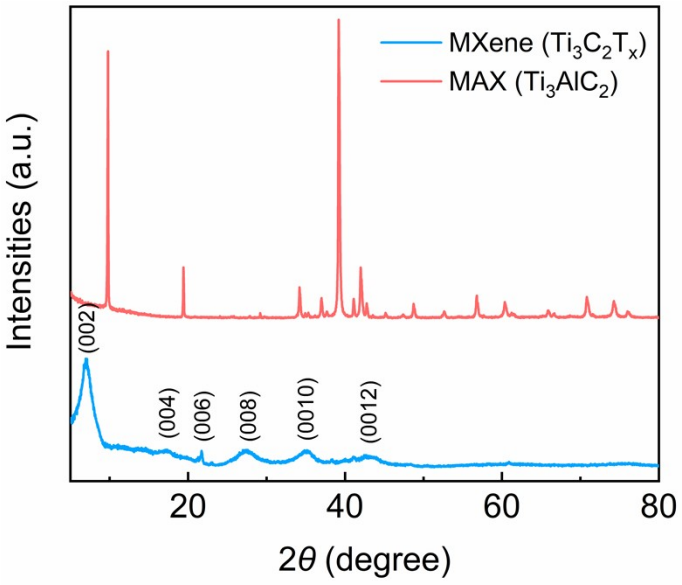

Figure S4. XRD pattern of MAX powder and MXene nanosheets.

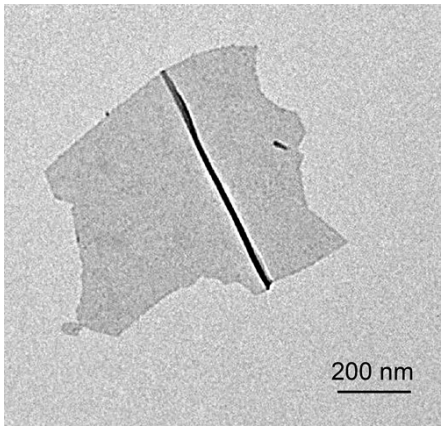

Figure S5. TEM image of MXene nanosheet.

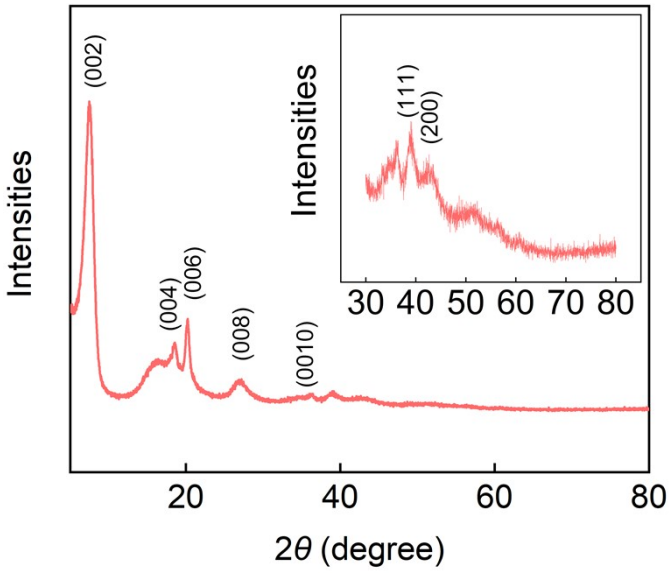

14

15 **Figure S6.** XRD pattern of Ag@MX. The peaks at 7.2°, 18.3°, 20°, 26.5°, and 38° indicate the

16 presence of MXene. Peaks at 39° and 42° indicate the formation of AgNPs.

17

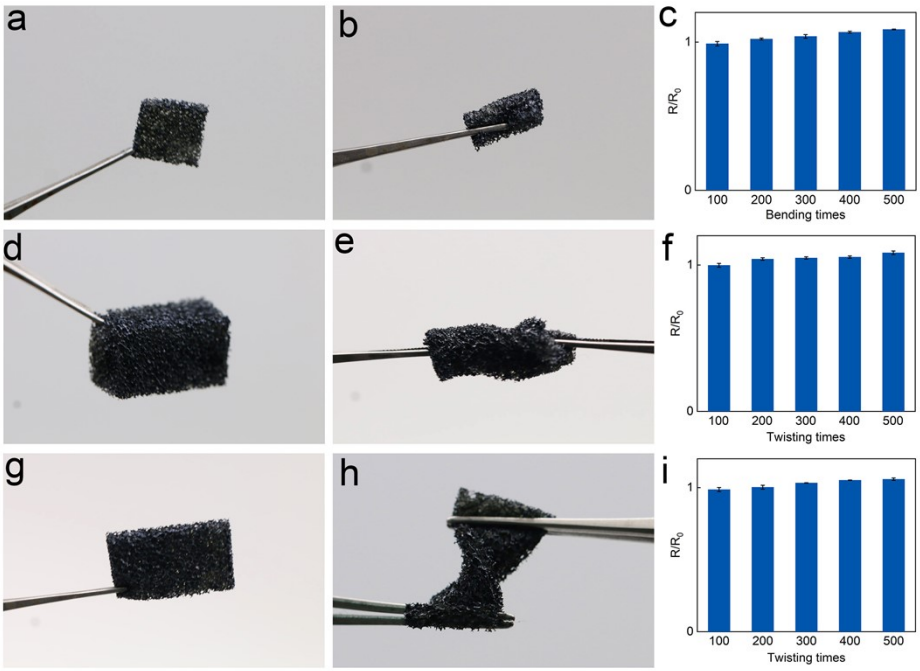

Figure S7. The illustration and resistance change of 3-Ag@MX@Sponge under bending and twisting status. (a, b) Pristine status and bending status of the 3-Ag@MX@Sponge (10 mm × 10 mm × 2 mm), (c) relative resistance of the 3-Ag@MX@Sponge after different times of bending. (d, e) Pristine status and twisting status of the 3-Ag@MX@Sponge (20 mm × 10 mm× 10 mm), (f) relative resistance of the 3-Ag@MX@Sponge after different times of twisting. (g, h) Pristine status and twisting status of the 3-Ag@MX@Sponge (20 mm× 10 mm× 2 mm), (i) relative resistance of the 3-Ag@MX@Sponge after different times of twisting.

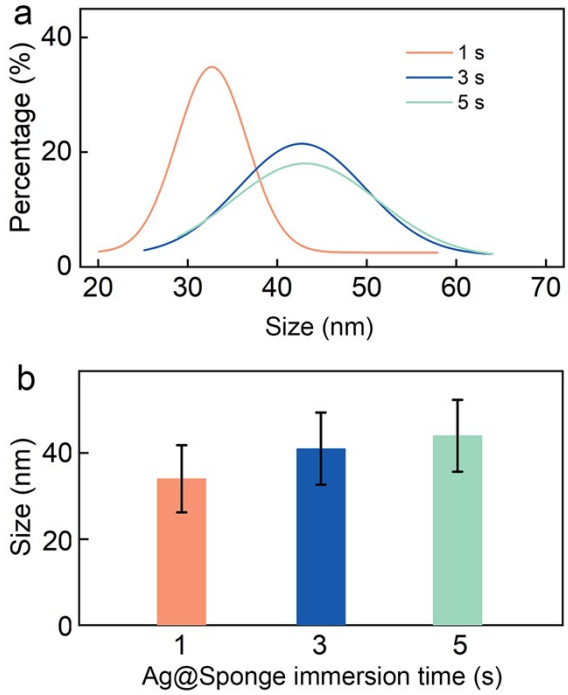

27

28 **Figure S8.** The diameter distribution (a) and the average size (b) of AgNPs with different

29 immersing time in 1 mmol/L $AgNO_3$.

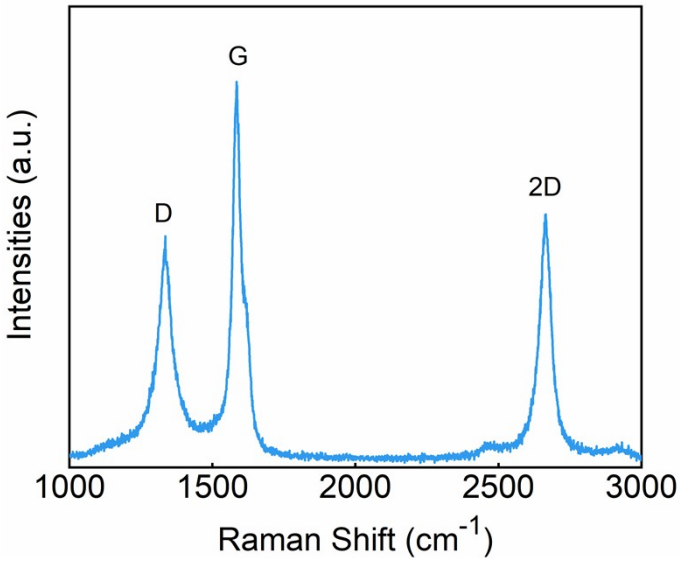

Figure S9. Raman spectra of LIG.

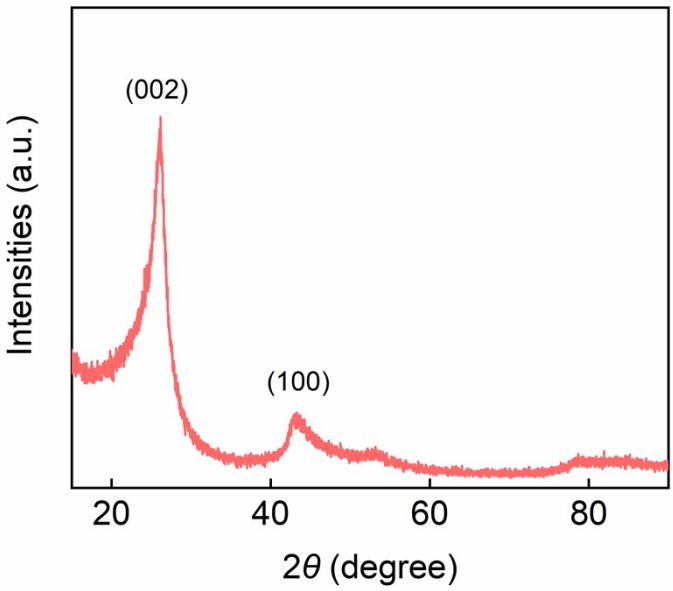

Figure S10. XRD pattern of LIG.

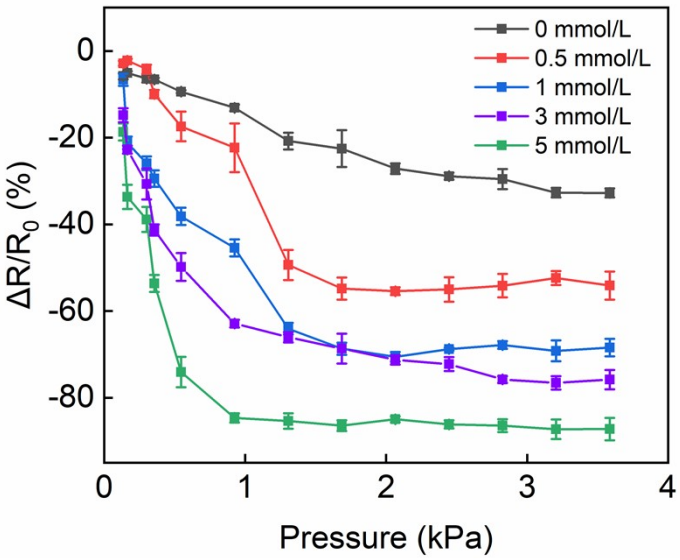

Figure S11. RRC of the sensors to different applied pressure. The sensors were fabricated by Ag@MX@Sponge with an immersing time of 3 s in 0, 0.5, 1, 3, and 5 mmol/L $AgNO_3$ solution, respectively.

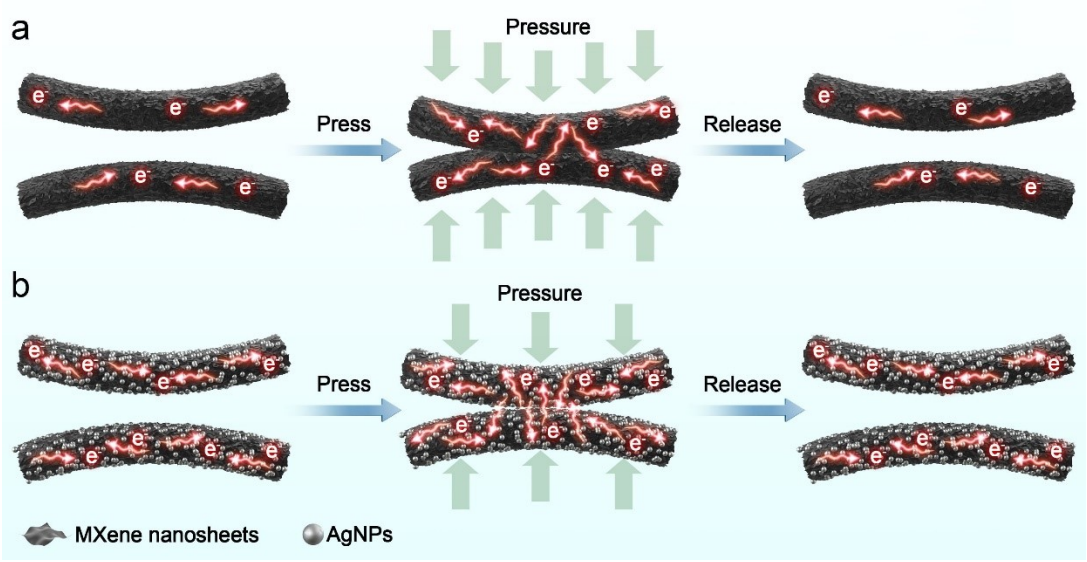

Figure S12. Schematic illustration showing the change of the number of conductive paths in the (a) MX@Sponge and (b) Ag@MX@Sponge with or without external pressure.

Note S1. The sensing mechanisms of MX@Sponge sensor and Ag@MX@Sponge sensor are illustrated in **Figure S12**. The compressive deformation under external pressure results in the formation of percolative network-that is, conductive paths are unavailable till the critical threshold of certain volume fractions of conductive agent is met in MX@Sponge.[1-3] Upon further compression, the conductive network becomes more developed in a given volume of the sponge while more contacts are formed between the sponge and the LIG-based interdigitated electrode, leading to much decreased sensor resistance (**Figure S12a**). When the pressure further increases, the number of the conductive paths becomes saturated, leading to stable resistance of the sensor. Once the pressure is released, the deformation of the sponge restores and the sensor resistance increases to the original value. The decoration of AgNPs on the MX@Sponge increases the sensitivity and the maximum RRC of the sensor. This significant improvement can be attributed to the contact between the AgNPs on the backbones. In MX@Sponge sensor, the contact between MXene nanosheets contributes to the change of the resistance. The surface of MX@Sponge becomes “rough” once coated with AgNPs. Therefore, even at a lower pressure, the AgNPs touch with each other and increase the number of conductive paths, thus leading to a higher sensitivity compared with the MX@Sponge sensor (**Figure S12b**). By controlling the growing time of AgNPs, the sensitivity of the Ag@MX@Sponge sensor can be tunable. A higher growing density of AgNPs correspond to a higher sensitivity of the sensor.

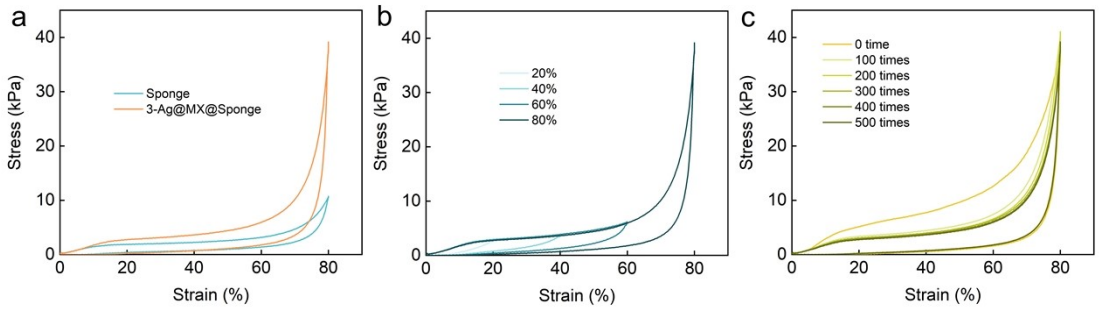

Figure S13. (a) The compressive strain-stress curves of Sponge and 3-Ag@MX@Sponge under 80% compression strain. (b) The compressive strain-stress curves of 3-Ag@MX@Sponge under different compression strain. (c) The compressive strain-stress curves of 3-Ag@MX@Sponge at 80% compression strain after being compressed for different times.

Note S2. Figure S13a shows the compressive strain-stress curves of Sponge and 3-Ag@MX@Sponge under 80% compression strain, respectively. The Ag@MX@Sponge perform higher compressive stress compared with pure sponge. **Figure S13b** indicates the compressive strain-stress curves of 3-Ag@MX@Sponge under different compression strain. **Figure S13c** shows the compressive strain-stress curves of 3-Ag@MX@Sponge at 80% compression strain after being compressed for different times. The compressive stress decreases after the first 100 compressing cycles. While during the following cycles, the sample shows similar compressive behavior. Such behavior also shows the good repeatability and durability of our wearable pressure sensor.

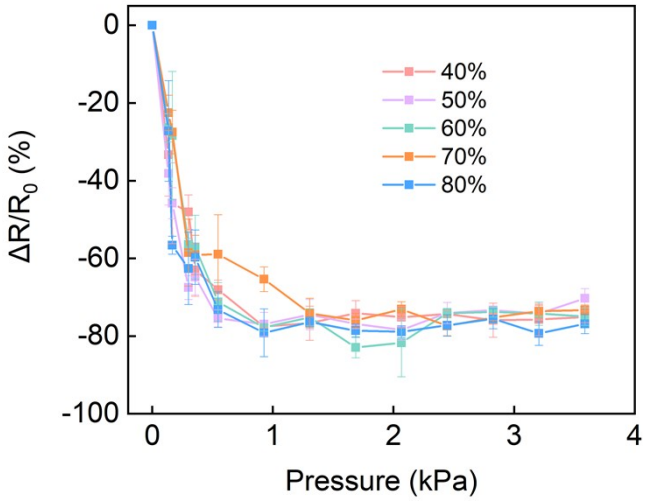

Figure S14. RRC of 3-Ag@MX@Sponge sensor to different pressure under various relative humidity.

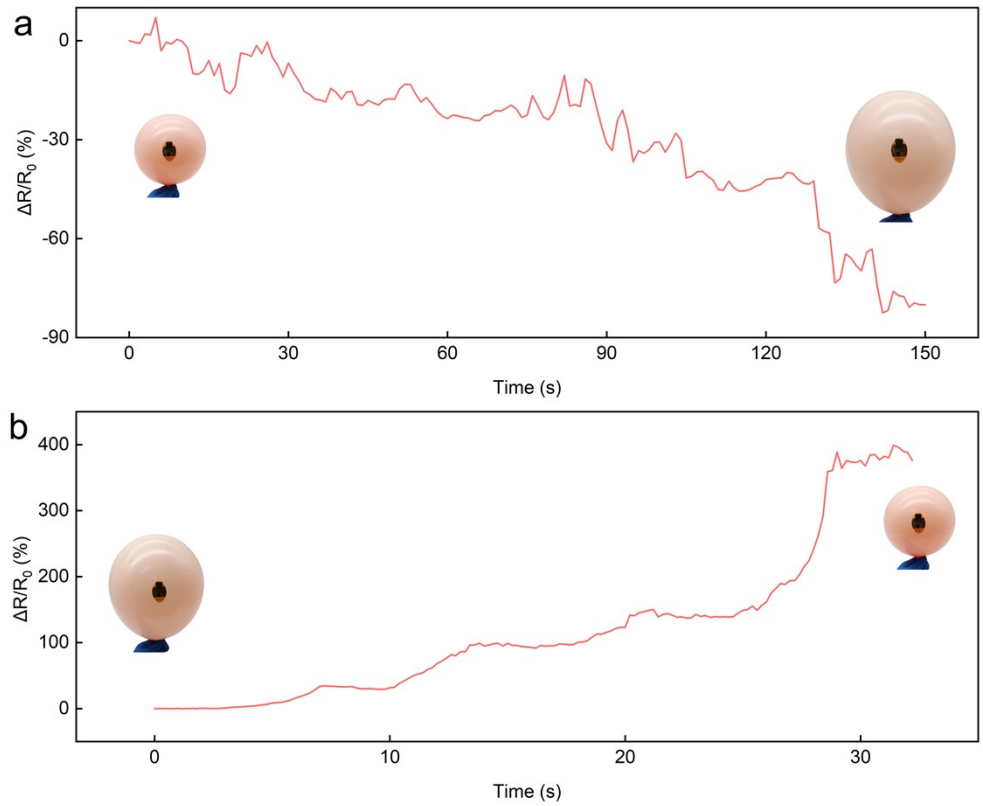

Figure S15. RRC of the sensor under inflating (a) and deflating (b) process of the balloon.

Note S3. Inflating process of the balloon is used to simulate the fruit growth. The PI film in this study is not stretchable and consequently the Ag@MX@Sponge cannot be stretched during inflating or deflating process, which eliminates the error by external tensing or relaxing. As shown in **Figure S15a**, the RRC shows a decreasing trend during inflating process. This phenomenon is attributed to the pressure exerted on the conductive sponge during the swelling of the balloon inflation. The RRC under deflating process of the balloon is demonstrated in **Figure S15b**. The obvious increasing trend of the resistance is observed, which is opposite to the inflating process. The simulation result indicates that the sensing chip prepared in this study has the potential to monitor the growth of fruits and vegetables or other agricultural products.

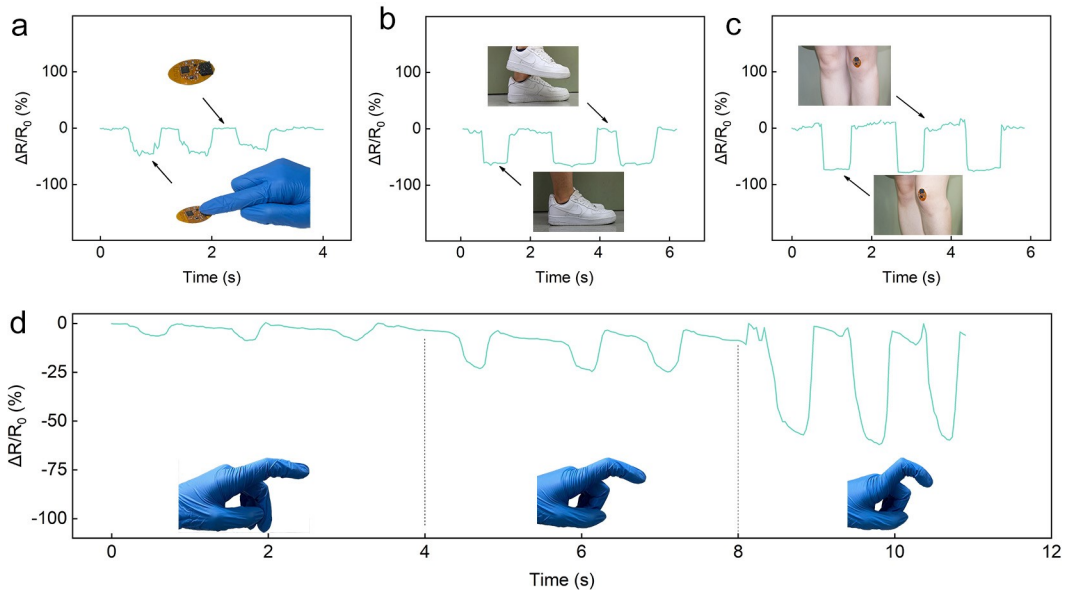

Figure S16. RRC of the 1-Ag@MX@Sponge sensor (f) finger pressing-releasing cycles, (g) foot stepping, (h) knee bending, (i) finger bending.

Note S4. We press the conductive sponge repeatedly with finger and the corresponding output signal is collected with results demonstrated in **Figure S16a**. The RRC decreases during compression and the variation is resulted from the uncontrollable finger pressure. Then, the chip is attached to the shoe sole to monitor the footsteps. As shown in **Figure S16b**, the sensing behavior is similar to finger pressing and shows good repeatability as well. The maximum RRC is more stable than finger pressing, which is attributed to the saturation of the conductive paths in conductive sponge under the pressure generated by foot stepping. Besides, the chip can also be used to monitor knee bending. As shown in **Figure S16c**, the RRC decreases when the knee is bending. During this process, the knee exerts pressure on the conductive sponge and the RRC shows an obvious decrease. We also use the chip to detect the finger bending. As shown in **Figure S16d**, the chip shows different response under different bending degrees and higher bending degrees result in a higher RRC.

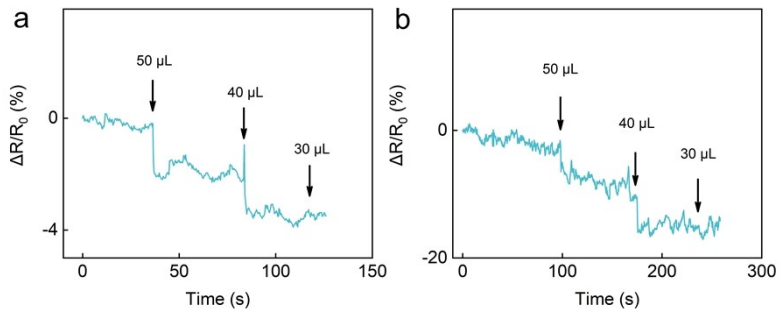

105

106 **Figure S17**. RRC of the (a) MX@Sponge sensor and (b) 3-Ag@MX@Sponge sensor under the

107 pressure generated by different amount of water drop.

108

Table S1. Normalized weight percentage of C, Ti, and Ag in Ag@MX@Sponge with different immersing time of MX@Sponge in 1 mmol/L $AgNO_3$.

Time/s	Ag/%	C/%	Ti/%
1	0.96	19.18	79.86
3	1.36	17.03	81.61
5	1.63	23.38	74.98

Table S2. Comparison of the sensitivity and linear detection range of Ag@MX@Sponge sensors with other reported sponge-based wearable pressure sensors.

Sensors	Sensitivity/kPa^{-1}	Linear detection range /kPa	Reference
Carbonized melamine sponge sensor	0.36	N/A	4
Carbon black-TPU sponge sensor	1.12	0–60	5
Graphene/AgNWs-coated sea sponge sensor	0.29	0–2.5	6
Reduced graphene oxide-PANI-based sponge sensor	0.77	<6	7
$CaCu_3Ti_4O_{12}$@PU sponge sensor	0.73 0.135	0–1.6 1.6–22.8	8
MXene@Chitosan@PU sponge sensor	0.014 0.015	<6.5 6.5–85.1	9
Graphene-based sponge sensor	1.04 0.12	0.013–0.26 0.26–20	10
Reduced graphene oxide-based sponge sensor	0.26 0.03	0–2 2–10	11
Reduced graphene oxide@PU sponge sensor	1.06 2.82	<40 40–58	12
MX@Sponge sensor	0.10	0.14–2.83	This work
1-Ag@MX@Sponge sensor	0.20	0.14–2.47	
3-Ag@MX@Sponge sensor	0.41	0.14–1.31	
5-Ag@MX@Sponge sensor	0.90	0.14–0.55	

TPU: thermoplastic polyurethane; PU: polyurethane; PANI: polyaniline; N/A: not available.

115 **Table S3.** Bill of components.

Components	Description	Footprint	Value and series number
C1, C4, C5	Capacitor	0402	1 μF
C2	Capacitor	0402	10 μF
C3, C8	Capacitor	0402	100 nF
D1	High Conductance Fast Diode	0402	Diode 1N4148
P1	Pin for sensor		3.937 mm pitch
P2	FPC/FFC connector		0.5 mm pitch
P3	Pin for power		2.54 mm pitch
R1, R2	Resistor	0402	10 kΩ
R3, R5	Resistor	0402	10 Ω
R4, R6	Resistor	0402	0
R_{ref}	Resistor	0402	200 kΩ
U1	LDO	SOT23-5	TPS7A05
U2	Microcontroller	QFN7X7-48	ESP32-PICO-D4
U3	ADC	MS10	LTC2421

116 FPC: flexible print circuit; FFC: flexible flat cable; LDO: low-dropout regulator; ADC: analog-to-
117 digital converter.

References

1. Y. Ma, Y. Yue, H. Zhang, F. Cheng, W. Zhao, J. Rao, S. Luo, J. Wang, X. Jiang, Z. Liu, N. Liu and Y. Gao, *ACS Nano*, 2018, **12**, 3209–3216.
2. Y. Wang, M. Chao, P. Wan and L. Zhang, *Nano Energy*, 2020, **70**, 104560.
3. M. Cao, S. Fan, H. Qiu, D. Su, L. Li and J. Su, *ACS Appl. Mater. Interfaces*, 2020, **12**, 36540–36547.
4. J. Yang, Y. Ye, X. Li, X. Lü and R. Chen, *Composites Sci. Technol.*, 2018, **164**, 187–194.
5. X. Guan, Z. Wang, W. Zhao, H. Huang, S. Wang, Q. Zhang, D. Zhong, W. Lin, N. Ding and Z. Peng, *ACS Appl. Mater. Interfaces*, 2020, **12**, 26137–26144.
6. X. Dong, Y. Wei, S. Chen, Y. Lin, L. Liu and J. Li, *Composites Sci. Technol.*, 2018, **155**, 108–116.
7. J. Huang, H. Wang, Z. Li, X. Wu, J. Wang and S. Yang, *J. Mater. Chem. C*, 2019, **7**, 7386–7394.
8. A. Chhetry, S. Sharma, H. Yoon, S. Ko and J. Y. Park, *Adv. Funct. Mater.*, 2020, **30**, 1910020.
9. X. P. Li, Y. Li, X. Li, D. Song, P. Min, C. Hu, H. B. Zhang, N. Koratkar and Z. Z. Yu, *J. Colloid Interface Sci.*, 2019, **542**, 54–62.
10. S. Chun, A. Hong, Y. Choi, C. Ha and W. Park, *Nanoscale*, 2016, **8**, 9185–9192.
11. H.-B. Yao, J. Ge, C.-F. Wang, X. Wang, W. Hu, Z.-J. Zheng, Y. Ni and S.-H. Yu, *Adv. Mater.*, 2013, **25**, 6692–6698.
12. Y. Tang, Q. Guo, Z. Chen, X. Zhang and C. Lu, *Composites Part A Appl. Sci. Manuf.*, 2019, **116**, 106–113.